JGR Space Physics

RESEARCH ARTICLE
10.1029/2022JA030967

Triggering of Whistler-Mode Rising and Falling Tone Emissions in a Homogeneous Magnetic Field

Yuya Fujiwara[1], **Yoshiharu Omura**[1], **and Takeshi Nogi**[1]

[1]Research Institute for Sustainable Humanosphere, Kyoto University, Kyoto, Japan

Key Points:

- Rising-tone and falling-tone emissions are generated simultaneously in a homogeneous magnetic field
- Electron holes and hills are formed in velocity phase space during the generation of rising and falling tone emissions, respectively
- Generation points of both emissions move upstream from the triggering wave

Correspondence to:

Y. Omura,
omura@rish.kyoto-u.ac.jp

Citation:

Fujiwara, Y., Omura, Y., & Nogi, T. (2023). Triggering of whistler-mode rising and falling tone emissions in a homogeneous magnetic field. *Journal of Geophysical Research: Space Physics*, *128*, e2022JA030967. https://doi.org/10.1029/2022JA030967

Received 7 SEP 2022
Accepted 4 JAN 2023

The copyright line for this article was changed on 28 JAN 2023 after original online publication.

Author Contributions:

Conceptualization: Yoshiharu Omura
Data curation: Yuya Fujiwara
Formal analysis: Yuya Fujiwara
Funding acquisition: Yoshiharu Omura
Investigation: Yuya Fujiwara, Takeshi Nogi
Methodology: Yoshiharu Omura, Takeshi Nogi
Project Administration: Yoshiharu Omura
Resources: Yoshiharu Omura
Software: Yuya Fujiwara, Yoshiharu Omura, Takeshi Nogi
Supervision: Yoshiharu Omura
Validation: Yuya Fujiwara
Visualization: Yuya Fujiwara
Writing – original draft: Yuya Fujiwara

Abstract We perform a self-consistent one-dimensional electromagnetic particle simulation with a uniform magnetic field and open boundaries. The plasma environment consists of cold isotropic electrons, energetic electrons, and immobile ions. The energetic electrons are initialized with a subtracted-Maxwellian distribution with temperature anisotropy. By oscillating external currents with a constant frequency $0.2\,f_{ce}$, where f_{ce} is the electron cyclotron frequency, a whistler-mode wave is injected as a triggering wave from the center of the simulation system, and we investigated the process of interactions between the triggering wave and energetic electrons. We find that both rising-tone and falling-tone emissions are triggered through the formation of an electron hole and an electron hill in the velocity phase space consisting of a parallel velocity and the gyro-phase angle of the perpendicular velocities. The rising-tone emission varies from $0.2\,f_{ce}$ to $0.4\,f_{ce}$, while the falling-tone varies from $0.2\,f_{ce}$ to $0.15\,f_{ce}$. The generation region of the rising-tone triggered emission starts near the injection point of the triggering wave and moves upstream generating new subpackets. The generation region of the falling-tone triggered emission also moves upstream generating new subpackets. The simultaneous formation of the electron hole and hill is identified by separating small and large wavenumber components corresponding to lower and higher frequencies, respectively, by applying the discrete Fourier transformation to the waveforms in space. Based on the simulation results of the whistler-mode triggered emissions, we conclude that the mechanism of frequency variation of whistler-mode chorus emissions works even in a uniform magnetic field.

Plain Language Summary We perform a particle-in-cell simulation for the generation of whistler-mode waves in a homogeneous magnetized plasma. In addition to cold electrons supporting the propagation of whistler-mode waves, we assume energetic electrons that can interact with the waves through cyclotron resonance. We find both rising-tone and falling-tone waves are excited from a triggering wave with a constant frequency. We analyze the velocity distribution function of energetic electrons and find the formation of both electron holes and hills in the velocity phase space. The mechanism of frequency variation and nonlinear wave growth of whistler-mode chorus emissions works even in a uniform magnetic field.

1. Introduction

More than half a century ago, very low frequency (VLF) emissions triggered by whistler-mode waves from the Morse code dashes were first reported (Helliwell et al., 1964). The observed new emissions were amplified with various frequency modulations, and the waves were called VLF triggered emissions. For understanding triggered emissions, active experiments have been conducted by transmitting coherent VLF waves from ground stations, for instance, the Siple station and the High Frequency Active Auroral Research Program (Gołkowski et al., 2010, 2019; Helliwell & Katsufrakis, 1974). The triggered emissions vary in frequency and are classified as rising-tone, falling-tone, and hooked-tone. The mechanism of this frequency sweep is one of the most puzzling problems in space physics, and the nonlinear wave-particle interaction via cyclotron resonance has been studied as a key factor in the generation of emissions.

In the space environment around the Earth, chorus emissions with rising and falling tones are generated naturally. Chorus emissions show various frequency changes similar to triggered emissions and share most of the same properties as triggered emissions (Helliwell, 1988; Helliwell et al., 1986). The major difference between triggered emissions and chorus emissions is the source of the triggering wave. For chorus emissions, linear growth due to the temperature anisotropy generates coherent triggering waves (Kennel & Petschek, 1966), and for triggered emissions, artificial signals become triggering waves. Numerical simulations with triggering waves provide us with powerful measures for the analyses of chorus emissions.

Writing – review & editing: Yuya Fujiwara, Yoshiharu Omura, Takeshi Nogi

Numerical experiments of whistler-mode wave-particle interaction have been performed for the examination of nonlinear processes causing frequency variations. The rising-tone emissions have been reproduced by electron hybrid simulations (Katoh & Omura, 2006; Tao et al., 2017) and full particle simulations (Hikishima et al., 2010; Nogi & Omura, 2022). Falling tone and hooked-tone have been also reproduced in simulations (Chen et al., 2022; Nogi et al., 2020; Nunn & Omura, 2012). These numerical simulations have contributed to the development of theory for the dynamics of the resonant electrons. The motion of the resonant electrons in phase space under the whistler-mode wave is described by a second-order nonlinear ordinary differential equation (Dysthe, 1971; Nunn, 1984; Omura, 2021; Omura et al., 1991), and controlled by two main factors, the frequency sweep rate, and the magnetic field gradient. These simulation studies have modeled the Earth's magnetic field, and the background magnetic field gradient has been recognized as an important factor to sustain the nonlinear wave growth away from the equator (Fujiwara et al., 2022; Omura et al., 2009). It is very essential to investigate the nonlinear processes in the equatorial region without a background magnetic field gradient, where the frequency sweep rate becomes the dominant factor controlling the nonlinear motion of the resonant electrons, for a complete understanding of the generation of the VLF emissions.

A recent simulation study (Wu et al., 2020) has shown that both rising-tone and falling-tone chorus emissions are generated in a homogeneous magnetic field. However, the generation processes are not identified clearly because of insufficient diagnostics of the simulation results. Although the generation process of the first subpacket of the triggered emission in the homogeneous magnetic field has been analyzed (Fujiwara et al., 2022), the continuous generation process of the subpackets was not reproduced because of the short simulation run. In this paper, we aim to understand the generation mechanism of both rising-tone and falling-tone triggered emissions in the homogeneous magnetic field with a longer time simulation run.

This study is organized as follows: We describe the explanation of the simulation model and settings in Section 2. In Section 3, we analyze the generation process of rising-tone and falling-tone emissions based on diagnostics of the resonant currents and resonant electrons dynamics in phase space. Finally, we summarize our simulation results and give discussion in Section 4.

2. Simulation Model and Settings

We conduct a self-consistent electromagnetic particle simulation with a uniform magnetic field by using Kyoto university ElectroMagnetic Particle cOde (KEMPO) developed by Omura and Matsumoto (1993), Omura (2007), and Nogi et al. (2020). The plasma environment consists of cold electrons and energetic electrons. The former is initialized with bi-Maxwellian distribution and the latter with subtracted-Maxwellian distribution. The subtracted-Maxwellian distribution assumed in the simulation is expressed by the following equation:

$$F(u_{\parallel}, u_{\perp}) = C_{\mathrm{N}} \exp\left(-\frac{u_{\parallel}^2}{2U_{\mathrm{th},\parallel}^2}\right)\frac{1}{1-\beta}\left\{\exp\left(-\frac{u_{\perp}^2}{2U_{\mathrm{th},\perp}^2}\right) - \exp\left(-\frac{u_{\perp}^2}{2\beta U_{\mathrm{th},\perp}^2}\right)\right\}, \quad (1)$$

where C_{N} is a normalization coefficient, and β is a subtraction ratio. The bi-Maxwellian distribution and subtracted-Maxwellian distribution are defined in momentum space ($u_{\parallel}$, $u_{\perp}$) where $u_{\parallel} = \gamma v_{\parallel}$, $u_{\perp} = \gamma v_{\perp}$, and $\gamma = \left[1 - \left(v_{\parallel}^2 + v_{\perp}^2\right)/c^2\right]^{-1/2}$, for velocities of electrons not to exceed the speed of light. By oscillating external currents, a whistler-mode wave is injected as a triggering wave in the plasma environment at the center of the simulation system. We investigate the process of interactions between the triggering wave and energetic electrons. The amplitude of the triggering wave is set as $B_{\mathrm{wi}} = 1.0 \times 10^{-3}\, B_0$, where B_0 is a background magnetic field, with frequency $\omega = 0.2\, \Omega_{\mathrm{e}}$, where Ω_{e} is an electron cyclotron frequency. The value of the amplitude is within the effective range which is obtained from the previous result for the formation of the coherent rising-tone triggered emissions in a parabolic magnetic field (Hikishima & Omura, 2012). The plasma frequency of cold electrons is set as $\omega_{\mathrm{pe}} = 4\, \Omega_{\mathrm{e}}$ which is the typical value in the magnetosphere outside the plasmapause, and the density ratio $N_{\mathrm{h}}/N_{\mathrm{c}}$ of energetic electrons to cold electrons is set as 1.2×10^{-2}. The parallel and perpendicular thermal momenta of energetic electrons are $U_{\mathrm{th},\parallel} = 0.25\, c$ and $U_{\mathrm{th},\perp} = 0.27\, c$, where c is the speed of light, and the energy range of the energetic electrons is 1–100 keV as shown in Figure 6a. The linear growth rate is maximized at $\omega = 0.188\, \Omega_{\mathrm{e}}$ with a value of $1.34 \times 10^{-3}\, \Omega_{\mathrm{e}}$, which is calculated by Kyoto University Plasma Dispersion Analysis Package (Sugiyama et al., 2015). Other parameters are shown in Table 1.

Table 1
Simulation Parameters

Parameter	Value
Grid spacing	0.025 $c\Omega_e^{-1}$
Length of the simulation region	307.2 $c\Omega_e^{-1}$
Time step	0.02 Ω_e^{-1}
Simulation time	20,971.52 Ω_e^{-1}
Electron charge to mass ratio $-e/m_0$	-1
Number of superparticles for cold electrons	268,435,456
Number of superparticles for energetic electrons	536,870,912
Plasma frequency of cold electrons ω_{pe}	4 Ω_e
Density ratio of energetic electrons to cold electrons N_h/N_c	1.2×10^{-2}
Subtraction ratio β	0.3
Thermal momenta of energetic electrons $U_{th,\parallel}$, $U_{th,\perp}$	0.25 c, 0.27 c
Initial temperature anisotropy $A = T_\perp/T_\parallel - 1$	0.166
Amplitude of the triggering wave B_{wi}	1.0×10^{-3} B_0
Frequency of the external current ω	0.2 Ω_e

As the boundary condition, a masking method of absorbing waves is applied to the simulation (Umeda et al., 2001). When the electrons pass the outer boundary, particles are reflected and their gyro phases are randomized so that the phase-organized electrons may not generate new emissions after the reflection. If the particles have pitch angles lower than 5° at the outer boundary, their velocities are initialized again and the particles are injected at the boundary as fresh particles. This pitch angle threshold is determined with reference to a loss cone angle at $L \sim 4$. Although there is no loss cone in a uniform magnetic field, we have implemented this boundary condition for the following reasons. Anomalous trapping that causes acceleration of low pitch angle particles (Kitahara & Katoh, 2019) is suppressed, and the fresh particles can cause a continuous generation of subpackets.

3. Simulation Results

Figure 1 shows the temporal and spatial evolution of wave magnetic field amplitudes B_w of (a) total waves, (b) backward waves, and (c) forward waves. For separating forward waves from backward waves, spatial helicities of the whistler-mode waves are used. In Figures 1b and 1c, we find that the triggered subpackets are generated mainly in the upstream region. They have amplitudes greater than that of the triggering waves. Similarly, triggered subpackets are formed as shown in Figures 1b and 1c because of the symmetry of the simulation setup with respect to the equator. Some minor differences (e.g., the amplitude of the subpacket and the timing of the generation) are due to the randomness of the initial particle distribution in phase space.

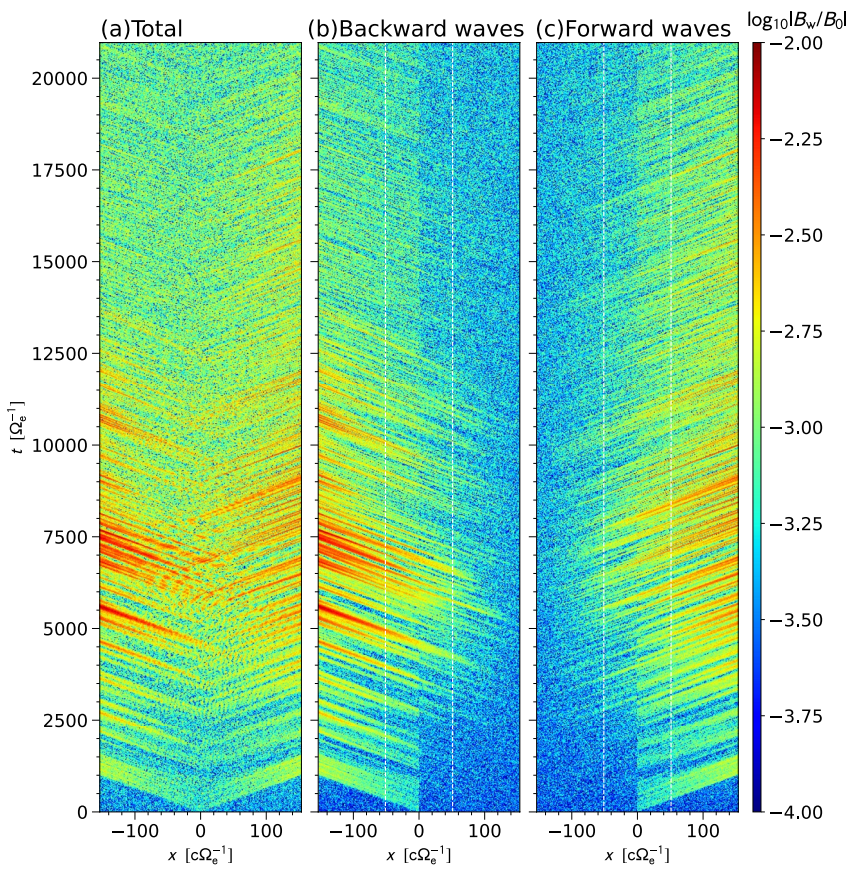

Figure 1. Temporal and spatial evolution of the magnetic field amplitude of (a)total waves, (b)backward waves, and (c) forward waves. White dashed lines indicate the positions $x = -51.2, 51.2\ c\Omega_e^{-1}$.

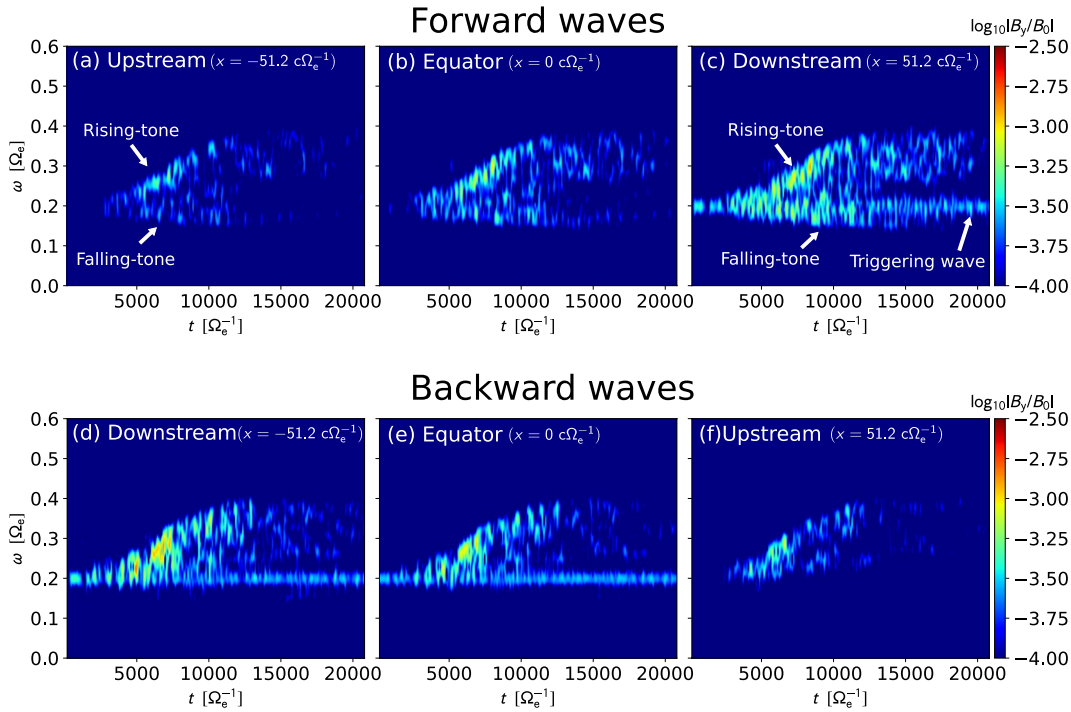

Figure 2. Spectrograms of both forward waves and backward waves at different positions at $x = -51.2, 0, 51.2\ c\Omega_e^{-1}$.

3.1. Dynamic Spectra at Different Positions

Figures 2a–2c show the spectra at different positions in the upstream region $\left(x = -51.2\ c\Omega_e^{-1}\right)$, the equator $\left(x = 0\ c\Omega_e^{-1}\right)$, and the downstream region $\left(x = 51.2\ c\Omega_e^{-1}\right)$ for forward waves, respectively. Multiple rising-tone elements and one falling-tone element are observed in Figures 2a–2c. The rising-tone elements sweep their frequency from $\omega = 0.2\ \Omega_e$ to $\omega = 0.4\ \Omega_e$. The falling-tone element sweeps its frequency from $\omega = 0.2\ \Omega_e$ to $\omega = 0.15\ \Omega_e$.

By taking frequency differences between two adjacent points along with the rising-tone emissions and falling-tone emissions in the dynamic spectra, we calculate frequency sweep rates. We obtain the average frequency sweep rate of the rising-tone emission over the time period $t = 4000$–$11000\ \Omega_e^{-1}$ as $\partial\omega/\partial t = 2.16 \times 10^{-5}\ \Omega_e^2$ in the upstream region and $\partial\omega/\partial t = 2.21 \times 10^{-5}\ \Omega_e^2$ in the downstream region, respectively. We also obtain the average frequency sweep rate of the falling-tone emission over $t = 5000$–$11000\ \Omega_e^{-1}$ in the downstream region as $\partial\omega/\partial t = -3.98 \times 10^{-6}\ \Omega_e^2$ in the upstream region and $\partial\omega/\partial t = -4.72 \times 10^{-6}\ \Omega_e^2$ in the downstream region, respectively. The frequency sweep rates are of the same order of magnitude as in the simulation results for rising-tone emissions $\partial\omega/\partial t = 2.6 \times 10^{-4}\ \Omega_e^2$ (Tao et al., 2021), $9.0 \times 10^{-5}\ \Omega_e^2$ (Hikishima & Omura, 2012), $4.53 \times 10^{-5}\ \Omega_e^2$ (Katoh & Omura, 2006), and $1.49 \times 10^{-6}\ \Omega_e^2$ (Nunn et al., 2005).

Figures 2d–2f also show the spectra at different positions in the downstream region, the equator, and the upstream region for backward waves, respectively. Rising-tone elements are observed but falling-tone elements are not observed. The difference between forward waves and backward waves is caused by the randomness of the initial particle distribution in the velocity phase space. In order to focus on the difference between the generation processes of rising-tone and falling-tone in this paper, we analyze the formation processes of rising-tone and falling-tone emissions for forward waves.

3.2. Separation of Rising-Tone and Falling-Tone Based on Wavenumber Spectra

Figures 2a–2c show multiple rising-tone elements and a falling-tone element. Rising-tone elements and falling-tone elements can be separated by the different frequency ranges by applying band-pass filters in the frequency domain. However, the frequency resolution is restricted by the window length in time. For accurate

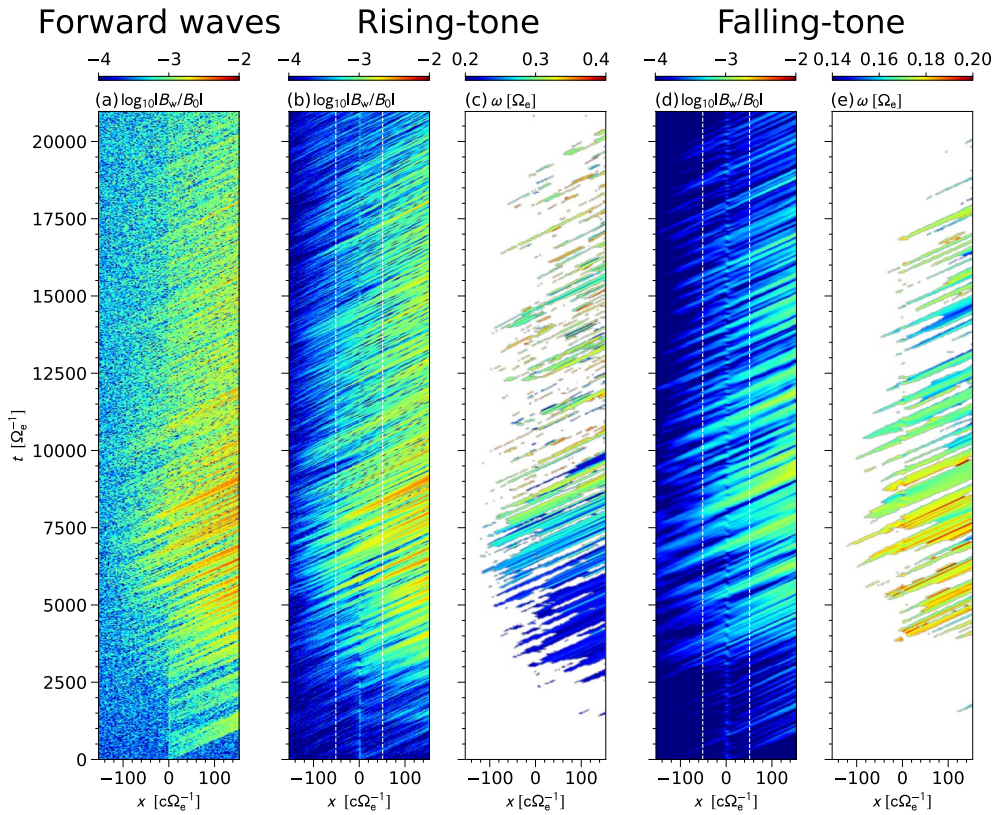

Figure 3. Temporal and spatial evolution of the magnetic field amplitude of forward waves with different wavenumber ranges (a) all wavenumbers (all frequencies) (b)k = 2.07–3.65 $c^{-1}\Omega_e$ (ω = 0.21–0.45 Ω_e), and (d)k = 1.34–1.95 $c^{-1}\Omega_e$ (ω = 0.10–0.19 Ω_e). The wavenumber ranges of (b) and (d) are corresponding to the rising-tone element and falling-tone element, respectively. Instantaneous frequency for the rising-tone element is shown in (c) and that for the falling-tone element is shown in (e). White dashed lines indicate the positions $x = -51.2, 51.2\ c\Omega_e^{-1}$.

analyses of wave-particle interactions, one wave packet should be extracted from multiple wave packets without the post-processing in time so that correlation analyses of the wave and particles can be processed at each time step in the simulation. The real-time wave separation is achieved by applying band-pass filters in the wavenumber domain using the discrete Fourier transform (DFT) under the assumption of the constant dispersion relation of whistler-mode waves in the uniform magnetic field and the uniform cold plasma density as assumed in the present simulation model.

Figures 3a, 3b, and 3d show the temporal and spatial evolution of the wave magnetic field amplitude B_w for forward waves with different wavenumber ranges. Figure 3a includes all wavenumbers, Figure 3b shows waves with k = 2.07–3.65 $c^{-1}\Omega_e$ corresponding to ω = 0.21–0.45 Ω_e, and Figure 3d shows waves with k = 1.34–1.95 $c^{-1}\Omega_e$ corresponding to ω = 0.10–0.19 Ω_e, respectively. Some wave packets appear to be staying in the center of Figures 3b and 3d, but these wave packets have appeared as a result of the DFT of the discontinuity point of the triggering wave injection place.

Figures 3c and 3e show the temporal and spatial evolution of instantaneous frequencies for forward waves with different wavenumber ranges. The instantaneous frequency is calculated from the phase variation of the transverse wave magnetic field (Nogi & Omura, 2022). If the amplitude value is less than $10^{-3.5}$, it is masked with white color. In Figure 3b, we find the subpackets generation with the gradual frequency increase ω = 0.2–0.4 Ω_e during t = 2,000–10, 000 Ω_e^{-1}. After t = 12, 000 Ω_e^{-1}, the wave packet with frequency ω = 0.3–0.4 Ω_e are generated intermittently. In Figure 3e, we find the subpackets generation with the gradual frequency decrease ω = 0.2–0.14 Ω_e during t = 3000–12000 Ω_e^{-1}.

In a recent study, Nogi and Omura (2022) have shown that the source region of the first long subpacket triggered by an injected wave moves with the source velocity $V_s = V_g + V_R$. In the frequency range of ω = 0.14–0.4 Ω_e,

V_s becomes negative as shown in figure 10 of Nogi and Omura (2022). Although the triggered subpackets of both rising and falling tone emissions are relatively short in comparison with the long subpacket of Nogi and Omura (2022), they are generated in the upstream region from the triggering wave, and this result is in agreement with the model that the upstream motion of the generation point is due to the negative value of V_s. After $t = 7,500\ \Omega_e^{-1}$, however, the generation of subpackets becomes less frequent, and the motion of the generation region almost stops.

3.3. Calculation of Inhomogeneous Factor *S*

The motion of a resonant electron in velocity phase space interacting with a coherent whistler-mode wave is described by the following set of differential Equations 2 and 3 as

$$\frac{d\zeta}{dt} = \theta, \tag{2}$$

$$\frac{d\theta}{dt} = \omega_{tr}^2(\sin\zeta + S), \tag{3}$$

where $\theta = k(v_{\parallel} - V_R)$ and ζ is a relative phase angle between the wave magnetic field B_w and the perpendicular velocity of an electron $v_{\perp}$(Omura, 2021). The parameter S is an inhomogeneity factor given by

$$S = -\frac{s_1}{s_0 \omega \Omega_w}\frac{\partial \omega}{\partial t}, \tag{4}$$

where $\Omega_w = eB_w/m_0$. The parameters s_0 and s_1 are given by

$$s_0 = \frac{\chi}{\xi}\frac{V_{\perp 0}}{c}, \tag{5}$$

and

$$s_1 = \gamma\left(1 - \frac{V_R}{V_g}\right)^2, \tag{6}$$

where $V_{\perp 0}$ is an average perpendicular velocity. The parameters χ and ξ are given by $\chi^2 = 1/(1 + \xi^2)$ and $\xi^2 = \omega(\Omega_e - \omega)/\omega_{pe}^2$, respectively. If the magnetic field gradient is included in the derivation, S has another term $\partial\Omega_e/\partial x$. The constant ω_{tr} is the trapping frequency corresponding to the oscillation frequency of trapped resonant electrons in the velocity phase space. Motions of resonant electrons are divided into two main trajectories by the separatrix. Electrons inside the separatrix (trapped electrons) rotate stably with the order of the trapping frequency, but the trajectories of the electrons outside the separatrix (untrapped electrons) are distorted depending on S values. When $S \neq 0$, untrapped resonant electrons cross the resonance velocity in the limited range of ζ, while they cannot cross the resonance velocity when $S = 0$.

Using the obtained value of the average frequency sweep rate, we calculate S values using Equation 4. Figure 4 shows the time evolution of magnetic field amplitude, instantaneous frequency, and S values in the upstream region $\left(x = -51.2\ c\Omega_e^{-1}\right)$ and the downstream region $\left(x = 51.2\ c\Omega_e^{-1}\right)$ for the rising-tone emission and falling-tone emission, respectively. In Figures 4c and 4f, we find that the S values take approximately −0.4 to −0.2 for the rising-tone emission, and in Figures 4i and 4l, we find that the S values take approximately 0.1–0.3 for the falling-tone emission. The large fluctuations in S values are due to the large fluctuation of instantaneous frequency, and the instantaneous frequency becomes difficult to be determined accurately when the wave amplitude B_w becomes small.

In Figures 4c, 4f, 4i, and 4l, we find that $-1 < S < 1$, when and where triggered emissions are observed. The optimum inhomogeneity for nonlinear wave growth is at $S = |0.4|$ because the resonant current J_E takes the maximum value (Nunn & Omura, 2012; Omura et al., 2008). Our results show that the S becomes close to the optimum value for the nonlinear wave growth in agreement with the generation of rising-tone and falling-tone emissions. The generated wave packets undergo wave growth through propagation even in the downstream region where resonant currents are formed as described in the next subsection.

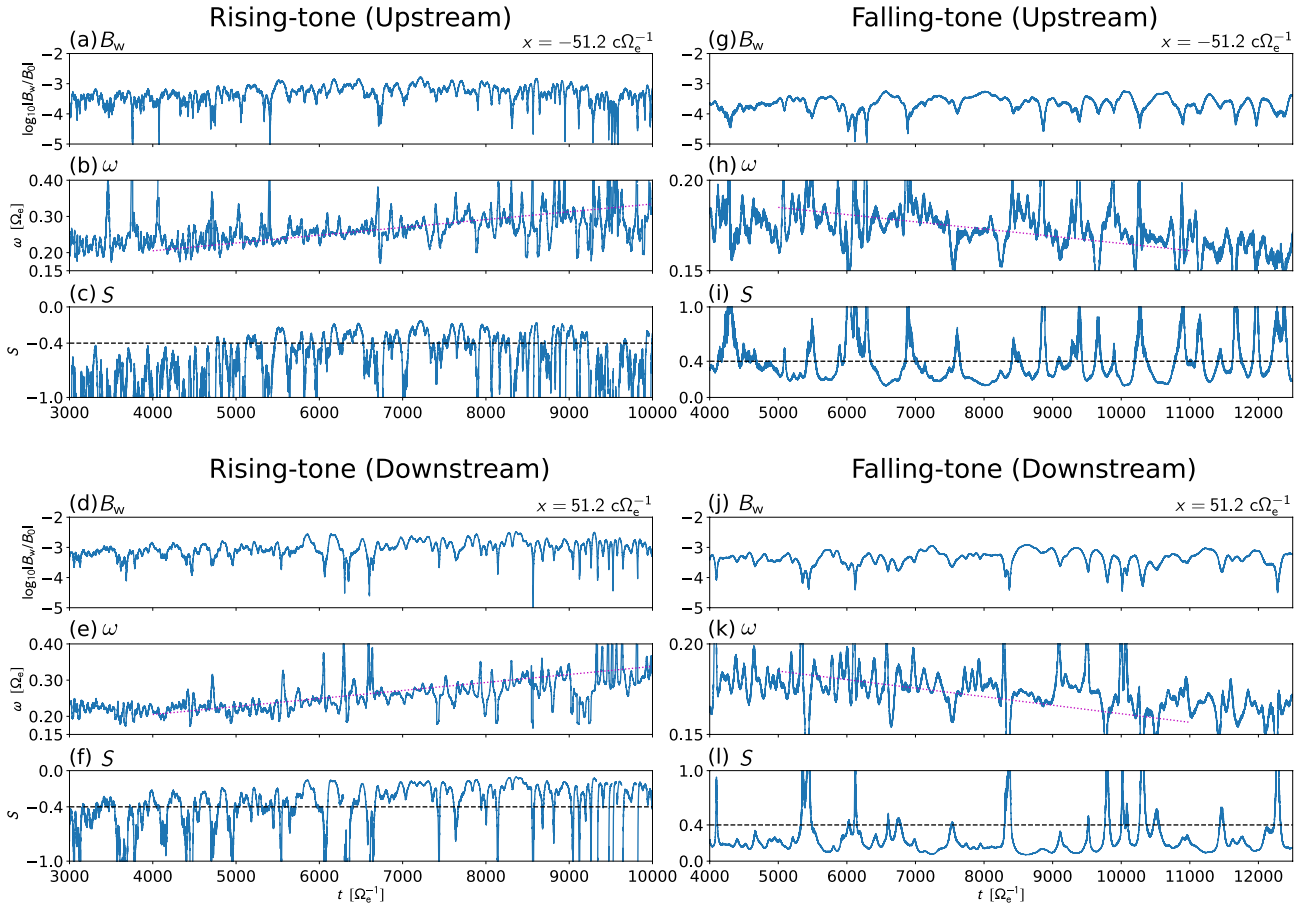

Figure 4. Time evolution of the magnetic field amplitude, instantaneous frequency, and S values observed at $x = -51.2\ c\Omega_e^{-1}$ and $x = 51.2\ c\Omega_e^{-1}$ for the rising-tone emission and falling-tone emission. Magenta dotted lines indicate average frequency sweep rate obtained from Figure 2 as $2.16 \times 10^{-5}\ \Omega_e^2$ in (b), $2.21 \times 10^{-5}\ \Omega_e^2$ in (e), $-3.98 \times 10^{-6}\ \Omega_e^2$ in (h), and $-4.72 \times 10^{-6}\ \Omega_e^2$ in (k), respectively.

3.4. Resonant Currents

We calculate resonant currents for understanding the generation process of rising-tone and falling-tone emissions in a homogeneous magnetic field. The resonant currents J_E and J_B are defined as currents parallel to the wave electric field and the wave magnetic field formed by resonant electrons, respectively. The wave equation describing the evolution of the wave amplitude B_w and the dispersion relation is modified by the resonant currents as described by

$$\frac{\partial B_w}{\partial t} + V_g \frac{\partial B_w}{\partial x} = \frac{\mu_0 V_g}{2}(-J_E), \tag{7}$$

$$c^2k^2 - \omega^2 - \frac{\omega\omega_{pe}^2}{\Omega_e - \omega} = \mu_0 c^2 k \frac{J_B}{B_w}, \tag{8}$$

where μ_0 is the vacuum permeability and V_g is the group velocity. The equations are derived from Maxwell's equations with the assumption that the transverse currents are decomposed into a resonant current formed by hot electrons and a cold electron current described by the momentum equation of the cold electron fluid. The detailed derivation is found in Appendix A of Omura et al. (2008).

Figures 5a and 5b show the temporal and spatial evolution of resonant currents for forward waves in the frequency range $\omega = 0.21$–$0.45\ \Omega_e$. To reduce the numerical noise, we only use the resonant part of energetic electrons with the parallel velocities $V_{R(0.21)} < v_\parallel < V_{R(0.45)}$, where $V_{R(\omega)}$ is a resonance velocity for wave frequency ω. If the wave amplitudes are less than $3.2 \times 10^{-4}\ B_0$, the current densities J_E and J_B/B_w are masked

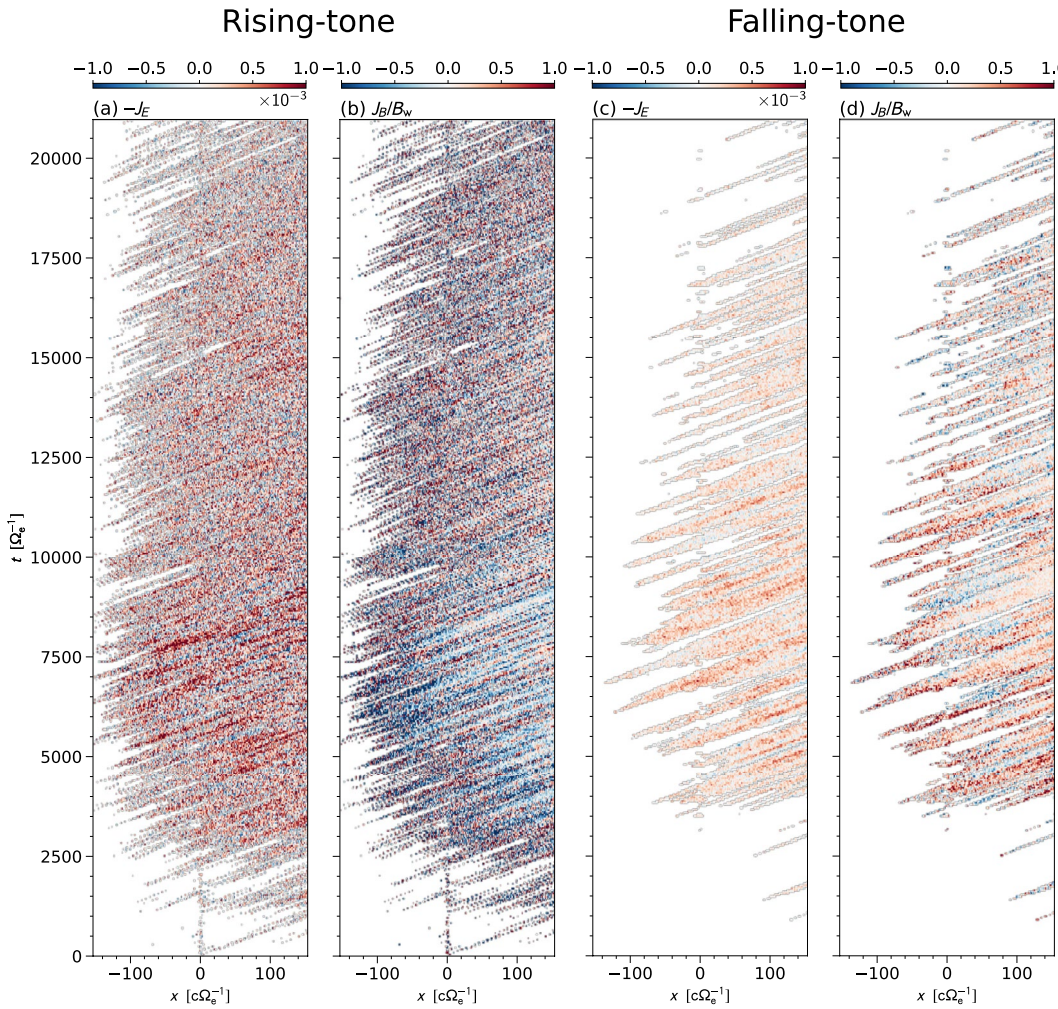

Figure 5. Temporal and spatial evolution of resonant currents of forward waves. (a)$-J_E$ and (b)J_B/B_w are calculated with reference to the rising-tone emission and (c)$-J_E$ and (d) J_B/B_w are calculated with reference to the falling-tone emission.

with white color, and this procedure is also the same for Figures 5c and 5d. During t = 3,000–9000 Ω_e^{-1} in a wide range in space, $-J_E$ becomes positive in Figure 5a. At $t = 3,000\ \Omega_e^{-1}$, $-J_E > 0$ takes place only in the downstream region, and the areas that satisfy $-J_E > 0$ expand to the upstream as well as the downstream during t = 5,000–8, 500 Ω_e^{-1}. In Figure 5b, J_B/B_w becomes negative in the downstream at $t = 3,000\ \Omega_e^{-1}$. During t = 3,000–8, 500 Ω_e^{-1} the areas that satisfy $J_B/B_w < 0$ moves upstream and keeps it localized in space. From Equations 7 and 8, we find that $-J_E > 0$ and $J_B/B_w < 0$ cause rising-tone triggered emissions. By the localization of $J_B/B_w < 0$, the generation region of the new subpacket is also localized and moves from the downstream region to the upstream region. The newly generated subpackets propagate to the downstream region with amplification due to $-J_E > 0$ as convective growth. The wave frequency does not change much as the wave propagates with the group velocity because of the small J_B/B_w, where B_w becomes large because of the convective growth in the downstream region.

Figures 5c and 5d show the temporal and spatial evolution of resonant currents for forward waves in frequency range ω = 0.10–0.19 Ω_e. To reduce the numerical noise, we use the resonant part of energetic electrons with parallel velocities $V_{R(0.10)} < v_{\parallel} < V_{R(0.19)}$. In Figure 5c, $-J_E$ becomes positive in a wide range in space and J_B/B_w becomes positive mainly in the upstream region near the equator during t = 3000–11000 Ω_e^{-1}. From Equations 7 and 8, we find that $-J_E > 0$ and $J_B/B_w > 0$ causes falling-tone triggered emissions. By the localization of $J_B/B_w > 0$ in the upstream, the generation region of the new subpacket is also localized.

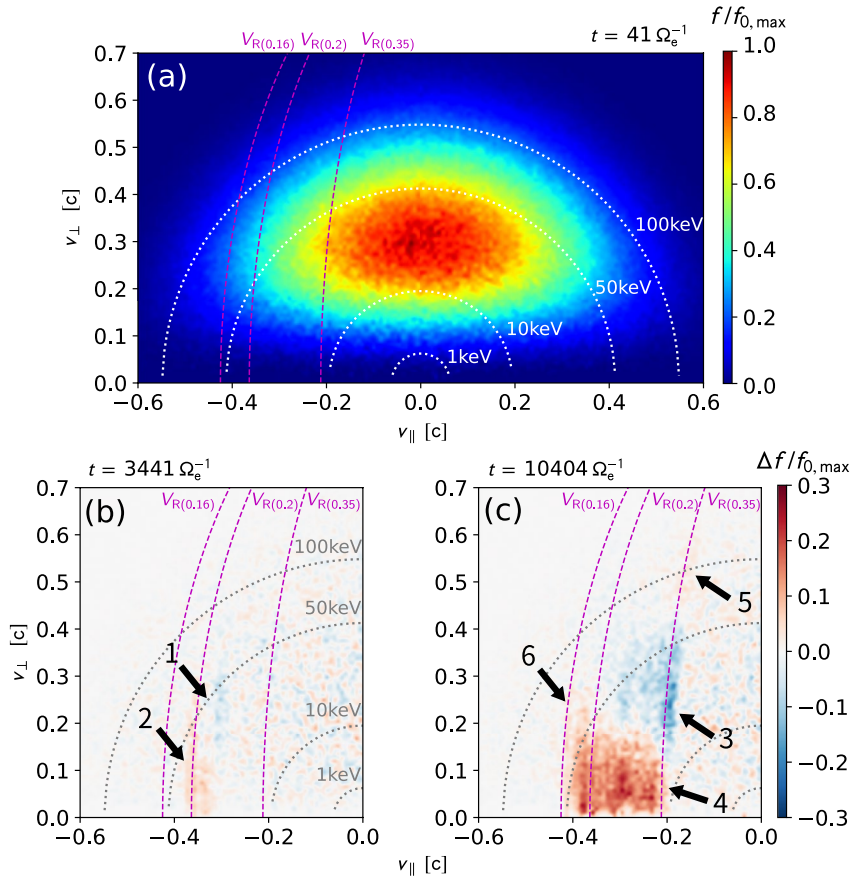

Figure 6. The velocity distribution function of the energetic electrons $f/f_{0,\max}$ and (b)–(c) $\Delta f/f_{0,\max}$, where $f_{0,\max}$ is the maximum initial value. The observation point is at $x = -51.2\ c\Omega_e^{-1}$. Magenta dashed curves indicate the resonance velocity. White and gray dotted semicircles indicate the energy range of the energetic electrons.

3.5. Time Evolution of the Velocity Distribution Function

Figure 6a shows the initial velocity distribution function where the values are normalized by the maximum initial value $f_{0,\max}$, and Figures 6b and 6c show the difference of the velocity distribution function from the initial values. The times in the panels are $t = 41, 3441, 10404\ \Omega_e^{-1}$, and the position is fixed at $x = -51.2\ c\Omega_e^{-1}$. Dashed magenta curves indicate the resonance velocities $V_{R(\omega)}$ for the frequencies $\omega = 0.16, 0.20, 0.35\ \Omega_e$, and the white and gray dotted semicircles indicate the constant energies of 1, 10, 50, and 100 keV.

In Figure 6b, we find a depression indicated by Arrow 1 on the right side of the dashed curve for $V_{R(0.2)}$ and an enhancement indicated by Arrow 2 on the left side of the dashed curve. The depression and the enhancement correspond to a decreased number of trapped electrons in the electron hole and an increased number of untrapped electrons scattered by the wave potential in velocity phase space, respectively. The untrapped electrons move around the separatrix of the wave potential, and they give their energies to the waves when they pass through near $\zeta = 3\pi/2$. Subsequently, the untrapped electrons lose their perpendicular velocity and are scattered to the lower pitch angles. By the continuous generation of the subpackets with frequency increase, the absolute value of the resonance velocity becomes smaller. In Figure 6c, we find that the depression expands to the right side of the dashed curve for $V_{R(0.35)}$ as indicated by Arrow 3, and the enhancement also expands on the left side of the dashed curve as indicated by Arrow 4. Because of the movement of the electron hole, 10–70 keV electrons are scattered to the lower pitch angles. In a higher pitch angle region indicated by Arrow 5 in Figure 6c, we find an enhancement which is originated from the trapped electrons. Some electrons in the electron hole are accelerated by receiving energy from waves and their energies reach over 100 keV. This acceleration process is explained by the following equation

$$\frac{dK}{dt} = -eV_{\perp 0}E_w S, \tag{9}$$

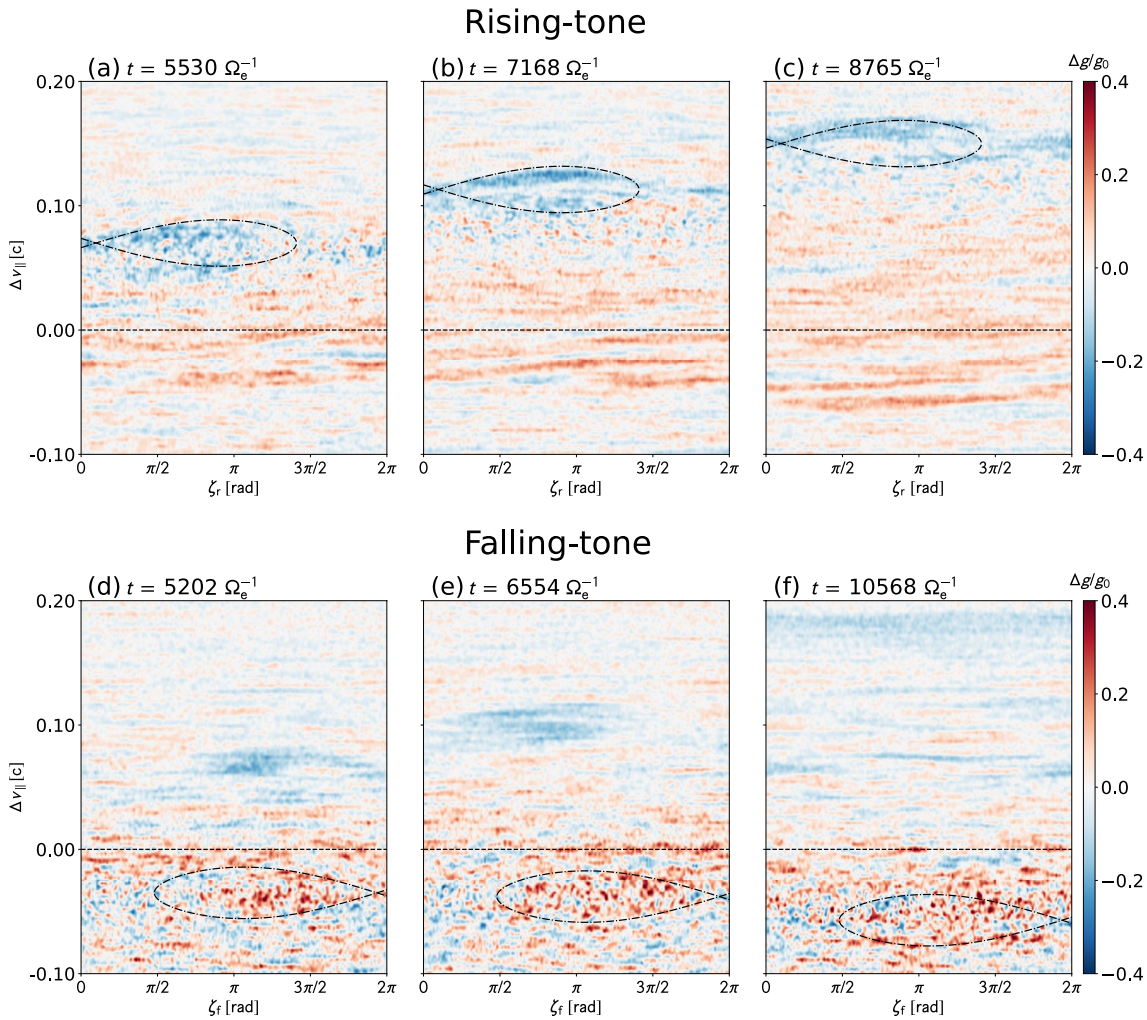

Figure 7. Time evolution of the phase space density of the energetic electrons $\Delta g/g_0 = (g - g_0)/g_0$ observed at $x = -51.2\ c\Omega_e^{-1}$. (a–c) are calculated with reference to the rising-tone emission and (d–f) are calculated with reference to the falling-tone emission.

where K is a kinetic energy of an electron (Omura, 2021). We find that the rising-tone emissions have a negative S value and the time variation of the kinetic energy of trapped electrons becomes positive, therefore the trapped electrons are accelerated.

The present result shows that the falling-tone emissions are generated after the generation of rising-tone emissions as seen in Figures 3b and 3d. As a possible generation mechanism of the falling-tone emission, a group of untrapped electrons is scattered to higher parallel velocities in magnitude with lower pitch angles by the rising-tone emissions as we find in Figures 6b and 6c, and they are bunched in gyro-phase, forming an electron hill in the lower density region of the velocity distribution function indicated by Arrow 6 in Figure 6c. As confirmed in the next subsection, the electron hill is formed near $\zeta = 3\pi/2$ with respect to a growing wave packet, resulting in positive $-J_E$ and positive J_B/B_w shown in Figures 5c and 5d. These resonant currents induce a self-sustaining falling-tone emission with multiple subpackets. The generation region of the falling-tone emissions is slightly downstream from that of the rising-tone emissions as we find in Figures 3b, 3d and 5.

3.6. Time Evolution of Phase Space Density of Energetic Electrons

Figures 7a–7f show differences in the phase space densities of energetic electrons from the initial densities at t = 5,530, 7,168, 8765 Ω_e^{-1} for Figures 7a–7c, and t = 5,202, 6,554, 10, 568 Ω_e^{-1} for Figures 7d–7f, respectively. The densities are normalized by the initial values g_0. The position is fixed at $x = -51.2\ c\Omega_e^{-1}$. The vertical axis

represents the difference between the parallel velocity of electrons and the resonance velocity calculated with the triggering wave frequency, and the formula is $\Delta v_{\parallel} = v_{\parallel} - V_R$. In the calculation of ζ_r, we use the reconstructed waveform of the transverse magnetic field containing waves with k = 2.07–3.65 $c^{-1}\Omega_e$ corresponding to the rising-tone element (ω = 0.21–0.45 Ω_e). In the calculation of ζ_f, we use the reconstructed waveform containing waves with k = 1.34–1.95 $c^{-1}\Omega_e$ corresponding to the falling-tone element (ω = 0.10–0.19 Ω_e). The reconstruction procedure is described in Section 3.2. Black dash-dotted lines in Figures 7a–7c indicate the separatrices calculated from simulation parameters in Table 1 and $S = -0.3$ obtained in Figure 4 with their centers at $\Delta v_{\parallel} = 0.07\ c$, 0.12 c, 0.15 c for Figures 7a–7c, respectively, obtained by visual inspection. Black dash-dotted lines in Figures 7d–7f also indicate the separatrices calculated from simulation parameters in Table 1 and $S = 0.2$ obtained in Figure 4 with their centers at $\Delta v_{\parallel} = -0.035\ c$, $-0.038\ c$, $-0.057\ c$ for Figures 7d–7f, respectively.

In Figures 7a–7c, we find that an electron hole structure appears with its center around $\zeta_r = \pi/2$ to π and moving upward as time elapses. By the presence of the electron hole, resonant currents become $-J_E > 0$ and $J_B < 0$. Under the electron holes, the enhancement appears, and the area of the enhancement spreads as the electron hole moves in the upward direction corresponding to a rising-tone emission. This enhancement is caused by the scattered electrons originating from untrapped resonant electrons outside the separatrix. Untrapped electrons give energy to the wave packets, generating the subpackets continuously. In Figures 7d–7f, on the other hand, an electron hill structure appears with its center around $\zeta_f = \pi$ to $3\pi/2$. The electron hill forms resonant currents $-J_E > 0$ and $J_B > 0$, resulting in the falling-tone emission, which corresponds to the downward motion of the hill in the velocity phase space. The absolute value of the resonance velocity becomes larger as the wave frequency decreases, and the flux of the resonant electrons becomes smaller. This makes the continuous generation of falling-tone subpackets difficult.

Figures 8a–8f show the time evolution of the differences of spatial distribution $h(x, \zeta)$ of energetic electron density from the initial densities, where the densities are normalized by the initial values h_0. For the calculation of h and h_0, the specific parallel velocity ranges are assumed: $v_{\parallel} = -0.29\ c$ to $-0.24\ c$ for Figures 8a–8b, $v_{\parallel} = -0.24\ c$ to $-0.14\ c$ for Figure 8c, and $v_{\parallel} = -0.44\ c$ to $-0.39\ c$ for Figures 8d–8f. These parallel velocity ranges of electrons to be counted is changed depending on the resonance velocity. The times of Figures 8a–8f correspond to those of Figures 7a–7f. In the calculation of ζ_r and ζ_f, the same procedure as in Figure 7 is used.

The area with negative $\Delta h/h_0$ is broadly distributed in space around $\zeta_r = \pi/2$ to π in Figures 8a–8c. This indicates that the electron hole forms a helical structure in space as well as the whistler-mode wave. The wave growth for the subpacket continues effectively because the electron holes are always maintained during the propagation of the subpacket from the upstream region to the downstream region. In Figures 8d–8f, on the other hand, the area with positive $\Delta h/h_0$ is distributed in space around $\zeta_f = \pi$ to $3\pi/2$, indicating that the electron hill with a helical structure is also formed in space.

4. Summary and Discussion

We performed the electromagnetic particle simulation of triggered emissions in the uniform magnetic field with the continuous triggering wave. The major findings are summarized below.

- Rising-tone and falling-tone triggered emissions are reproduced in the homogeneous magnetic field.
- By the presence of the electron hole, the resonant currents become $-J_E > 0$ and $J_B/B_w < 0$, and by the presence of the electron hill, the resonant currents become $-J_E > 0$ and $J_B/B_w > 0$. These resonant currents cause rising-tone and falling-tone emissions, respectively.
- The generation region of the rising-tone triggered emissions first appears near the injection point of the triggering wave and moves upstream generating new subpackets.
- The generation region of the falling-tone triggered emission also moves upstream generating new subpackets.

The nonlinear wave growth theory is constructed under the assumption of a single wave packet. When multiple waves are present as in our result, it is essential to separate them for accurate analysis, and only after the separation the correct resonant currents and relative angles ζ can be calculated. In the present analyses, we used wavenumber spectra to separate rising-tone and falling-tone emissions taking advantage of the uniform dispersion relation of whistle-mode waves in the homogeneous magnetic field.

The previous result of chorus simulation in a uniform magnetic field (Wu et al., 2020) shows that the generation of falling-tone emissions is more dominant than rising-tone emissions, which is not consistent with the present

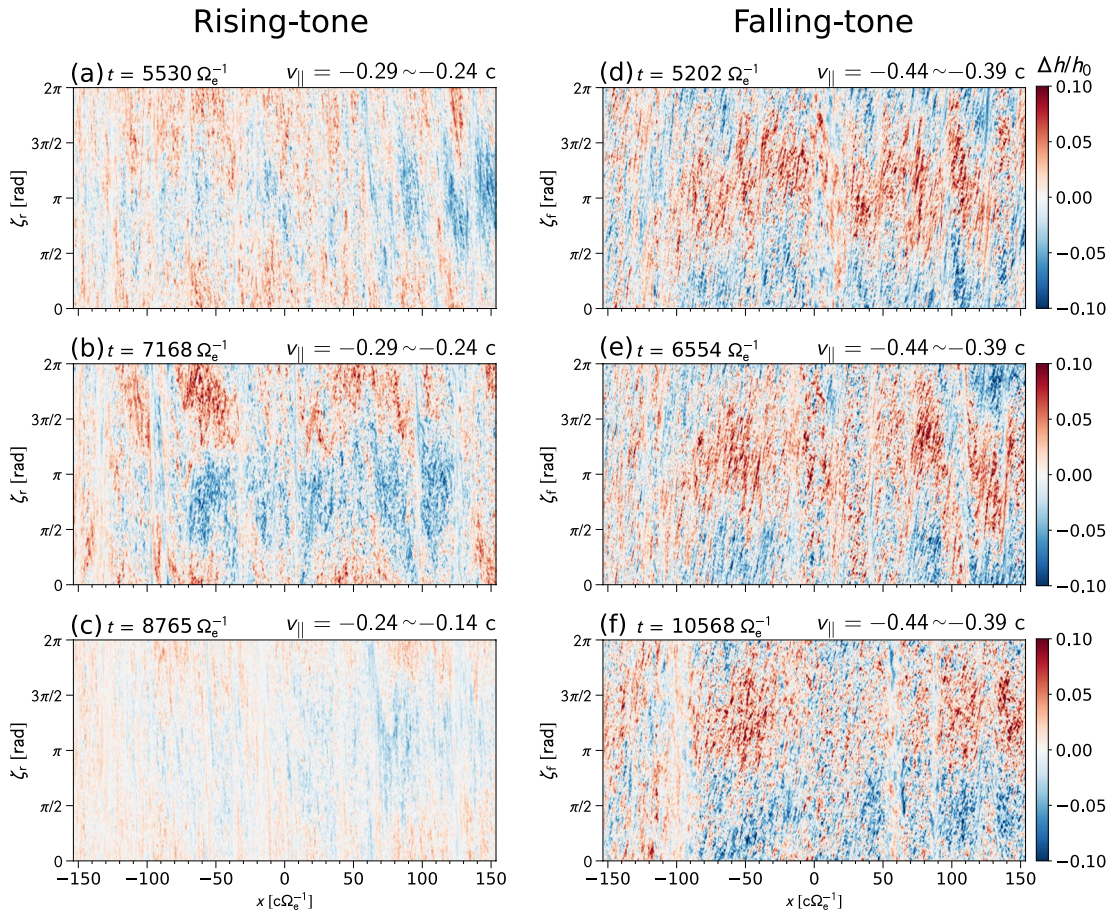

Figure 8. Time evolution of spatial distribution of relative angle ζ of the energetic electrons $\Delta h/h_0 = (h - h_0)/h_0$. (a–c) are calculated with reference to the rising-tone emission and (d–f) are calculated with reference to the falling-tone emission.

result. This difference is possibly caused by the initial velocity distribution of the energetic electrons. They adopt a bi-Maxwellian distribution as the initial velocity distribution, resulting in the large electron flux in lower pitch angles which can generate falling-tone emissions.

In the present homogeneous magnetic field model, we cannot determine the threshold wave amplitude, which can be determined in the parabolic magnetic field model (Omura et al., 2009). The triggering waves should be greater than the thermal fluctuation, which is determined by the number of super-particles in the simulation system. The threshold wave amplitude for the generation of the triggered emissions in the homogeneous magnetic field is a problem left as a future study.

Data Availability Statement

The simulation data files and a sample program to read the data files are open to the public on the web (https://doi.org/10.5281/zenodo.7003859). The simulation data used in this paper are obtained from the KEMPO1 code (http://space.rish.kyoto-u.ac.jp/software/).

Acknowledgments
The computer simulation in the present study was performed on the KDK computer system at Research Institute for Sustainable Humanosphere, Kyoto University. This work was supported by JSPS KAKENHI Grant JP17H06140.

References

Chen, H., Lu, Q., Wang, X., Fan, K., Chen, R., & Gao, X. (2022). One-dimensional gcPIC-df simulation of hooked chorus waves in the earth's inner magnetosphere. *Geophysical Research Letters*, *49*(4), e2022GL097989. https://doi.org/10.1029/2022GL097989

Dysthe, K. B. (1971). Some studies of triggered whistler emissions. *Journal of Geophysical Research*, *76*(28), 6915–6931. https://doi.org/10.1029/JA076i028p06915

Fujiwara, Y., Nogi, T., & Omura, Y. (2022). Nonlinear triggering process of whistler-mode emissions in a homogeneous magnetic field. *Earth Planets and Space*, *74*(95), 95. https://doi.org/10.1186/s40623-022-01646-x

Gołkowski, M., Harid, V., & Hosseini, P. (2019). Review of controlled excitation of non-linear wave-particle interactions in the magnetosphere. *Frontiers in Astronomy and Space Sciences*, *6*, 1-20. https://doi.org/10.3389/fspas.2019.00002

Gołkowski, M., Inan, U. S., Cohen, M. B., & Gibby, A. R. (2010). Amplitude and phase of nonlinear magnetospheric wave growth excited by the HAARP HF heater. *Journal of Geophysical Research*, *115*(A2), A00F04. https://doi.org/10.1029/2009JA014610

Helliwell, R. (1988). VLF wave-injection experiments from siple station, Antarctica. *Advances in Space Research*, *8*(1), 279–289. https://doi.org/10.1016/0273-1177(88)90373-0

Helliwell, R. A., Carpenter, D. L., Inan, U. S., & Katsufrakis, J. P. (1986). Generation of band-limited VLF noise using the siple transmitter: A model for magnetospheric hiss. *Journal of Geophysical Research*, *91*(A4), 4381–4392. https://doi.org/10.1029/JA091iA04p04381

Helliwell, R. A., Katsufrakis, J., Trimpi, M., & Brice, N. (1964). Artificially stimulated very-low-frequency radiation from the ionosphere. *Journal of Geophysical Research*, *69*(11), 2391–2394. https://doi.org/10.1029/jz069i011p02391

Helliwell, R. A., & Katsufrakis, J. P. (1974). VLF wave injection into the magnetosphere from siple station, Antarctica. *Journal of Geophysical Research*, *79*(16), 2511–2518. https://doi.org/10.1029/JA079i016p02511

Hikishima, M., & Omura, Y. (2012). Particle simulations of whistler-mode rising-tone emissions triggered by waves with different amplitudes. *Journal of Geophysical Research*, *117*(A4), A04226. https://doi.org/10.1029/2011JA017428

Hikishima, M., Omura, Y., & Summers, D. (2010). Self-consistent particle simulation of whistler mode triggered emissions. *Journal of Geophysical Research*, *115*(A12), A12246. https://doi.org/10.1029/2010JA015860

Katoh, Y., & Omura, Y. (2006). A study of generation mechanism of VLF triggered emission by self-consistent particle code. *Journal of Geophysical Research*, *111*(A12), A12207. https://doi.org/10.1029/2006JA011704

Kennel, C. F., & Petschek, H. E. (1966). Limit on stably trapped particle fluxes. *Journal of Geophysical Research*, *71*(1), 1–28. https://doi.org/10.1029/JZ071i001p00001

Kitahara, M., & Katoh, Y. (2019). Anomalous trapping of low pitch angle electrons by coherent whistler mode waves. *Journal of Geophysical Research: Space Physics*, *124*(7), 5568–5583. https://doi.org/10.1029/2019JA026493

Nogi, T., Nakamura, S., & Omura, Y. (2020). Full particle simulation of whistler-mode triggered falling-tone emissions in the magnetosphere. *Journal of Geophysical Research: Space Physics*, *125*(10), e2020JA027953. https://doi.org/10.1029/2020JA027953

Nogi, T., & Omura, Y. (2022). Nonlinear signatures of VLF-triggered emissions: A simulation study. *Journal of Geophysical Research: Space Physics*, *127*(1), e2021JA029826. https://doi.org/10.1029/2021JA029826

Nunn, D. (1984). The quasistatic theory of triggered VLF emissions. *Planetary and Space Science*, *32*(3), 325–350.

Nunn, D., & Omura, Y. (2012). A computational and theoretical analysis of falling frequency VLF emissions. *Journal of Geophysical Research*, *117*(A8), A08228. https://doi.org/10.1029/2012JA017557

Nunn, D., Rycroft, M., & Trakhtengerts, V. (2005). A parametric study of the numerical simulations of triggered VLF emissions. *Annales Geophysicae*, *23*(12), 3655–3666. https://doi.org/10.5194/angeo-23-3655-2005

Omura, Y. (2007). One-dimensional electromagnetic particle code KEMPO1: A tutorial on microphysics in space plasmas. In H. Usui & Y. Omura (Eds.), *Advanced methods for space simulations* (Terra Sci., 2007, pp. 1–21).

Omura, Y. (2021). Nonlinear wave growth theory of whistler-mode chorus and hiss emissions in the magnetosphere. *Earth Planets and Space*, *73*(1), 1–28. https://doi.org/10.1186/s40623-021-01380-w

Omura, Y., Hikishima, M., Katoh, Y., Summers, D., & Yagitani, S. (2009). Nonlinear mechanisms of lower-band and upper-band VLF chorus emissions in the magnetosphere. *Journal of Geophysical Research*, *114*(A7), A07217. https://doi.org/10.1029/2009JA014206

Omura, Y., Katoh, Y., & Summers, D. (2008). Theory and simulation of the generation of whistler-mode chorus. *Journal of Geophysical Research*, *113*(A4), A04223. https://doi.org/10.1029/2007JA012622

Omura, Y., & Matsumoto, H. (1993). KEMPO1: Technical guide to one-dimensional electromagnetic particle code. In H. Matsumoto & Y. Omura (Eds.),*Computer space plasma physics: Simulation Techniques and Softwares* (Terra Sci., 1993, pp. 21–65).

Omura, Y., Nunn, D., Matsumoto, H., & Rycroft, M. (1991). A review of observational, theoretical and numerical studies of VLF triggered emissions. *Journal of Atmospheric and Terrestrial Physics*, *53*(5), 351–368.

Sugiyama, H., Singh, S., Omura, Y., Shoji, M., Nunn, D., & Summers, D. (2015). Electromagnetic ion cyclotron waves in the earth's magnetosphere with a kappa-Maxwellian particle distribution. *Journal of Geophysical Research: Space Physics*, *120*(10), 8426–8439. https://doi.org/10.1002/2015JA021346

Tao, X., Zonca, F., & Chen, L. (2017). Identify the nonlinear wave-particle interaction regime in rising tone chorus generation. *Geophysical Research Letters*, *44*(8), 3441–3446. https://doi.org/10.1002/2017GL072624

Tao, X., Zonca, F., & Chen, L. (2021). A "trap-release-amplify" model of chorus waves. *Journal of Geophysical Research: Space Physics*, *126*(9), e2021JA029585. https://doi.org/10.1029/2021JA029585

Umeda, T., Omura, Y., & Matsumoto, H. (2001). An improved masking method for absorbing boundaries in electromagnetic particle simulations. *Computer Physics Communications*, *137*(2), 286–299. https://doi.org/10.1016/S0010-4655(01)00182-5

Wu, Y., Tao, X., Zonca, F., Chen, L., & Wang, S. (2020). Controlling the chirping of chorus waves via magnetic field inhomogeneity. *Geophysical Research Letters*, *47*(10), e2020GL087791. https://doi.org/10.1029/2020GL087791